Processing and properties of arsenic trisulfide chalcogenide glasses for direct laser writing of 3D micro-structures

Casey M. Schwarz[a], Henry E. Williams[a], Chris N. Grabill[a], Anna M. Lewis[a],
Stephen M. Kuebler[a,b,c,*], Benn Gleason[c], and Kathleen A. Richardson[c],
Alexej Pogrebnyakov[d], and Theresa S. Mayer[d],
Christina Drake[e], and Clara Rivero-Baleine[e]

[a]Chemistry Department, University of Central Florida, Orlando, FL 32816, USA
[b]Physics Department, University of Central Florida, Orlando, FL 32816, USA
[c]CREOL, The College of Optics and Photonics, University of Central Florida, Orlando, FL 32816, USA
[d]Department of Electrical Engineering, Pennsylvania State University, University Park, PA 16802, USA
[e]Lockheed Martin ~~Missiles and Fire Control~~, Orlando, FL 32819, USA

*kuebler@mail.ucf.edu; Tele: +1 407-823-3720; Fax: +1 407-823-2252; http://npm.creol.ucf.edu

ABSTRACT

Arsenic trisulfide (As_2S_3) is a~~n infrared (IR)~~ transparent material from ~620 nm to 11 µm, with direct applications in ~~IR~~ sensors, photonic waveguides, and acousto-optics. As_2S_3 may be thermally deposited to form glassy films of molecular chalcogenide (ChG) clusters. It has been shown that linear and multi-photon exposure can be used to photo-pattern thermally deposited As_2S_3. Photo-exposure cross-links the film into a network solid. Treating the photo-patterned material with a polar-solvent removes the unexposed material leaving behind a structure that is a negative-tone replica of the photo-pattern. In this work, nano-structure arrays were photo-patterned in As_2S_3 films by multi-photon direct laser writing (DLW) and the resulting structure, morphology, and chemical composition were characterized and correlated with the conditions of the thermal deposition, patterned irradiation, and etch processing. Raman spectroscopy was used to characterize the chemical structure of the unexposed and photo-exposed material, and near infrared ellipsometry was used to measure the refractive index. Physical characterization including structure size and surface adhesion of nano-scale features is related to the processing conditions.

Keywords: ~~Infrared optics,~~ arsenic trisulfide, chalcogenide glass, multi-photon, direct laser writing, microstructures.

1. INTRODUCTION

~~Infrared (IR)~~ Arsenic trisulfide (As_2S_3) optics have many applications including sensors, photonic waveguides, and acousto-optics ~~detectors, sensors and imaging systems~~. Producing light-weight, low-profile, robust optics with good thermal properties as well as lowering the cost and time for manufacturing are important goals to realize many of these applications. Conventional infrared (IR) optics are bulky, heavy, and expensive because they are often composed of costly single-crystal materials such as Ge, Si, or ZnSe[1-4]. Conventional processing techniques, such as diamond turning, also adds cost to the production while less expensive alternatives such as precision glass molding, produces heavy optics with limited functionality[5]. These factors complicate ~~frustrate~~ ~~high volume commercial~~ production of optical systems.

Chalcogenide glasses (ChGs) are multi-component materials that can be produced and processed more quickly with less expense than single-component crystalline IR optics. Multicomponent ChGs can be made to have a lower

change in refractive index with temperature (*dn*/*dt*) than single-component glasses. High coefficient of thermal expansion (CTE) can lead to component failure through delamination and make temperature control necessary. With multi-component ChGs, the CTE can be compositionally-tailored for high temperature ranges ~~applications~~.

As_2S_3 is a ChG that is transparent in the IR (620 nm to 11 µm) with applications in IR sensors, photonics waveguides, and acousto-optics[6]. As_2S_3 can be thermally deposited as thin films. Such films can be photo-patterned, like polymeric photo-resists, then chemically etched to obtain a targeted structure[7-10]. Three-dimensional (3D) structures such as woodpile photonic crystals, nanowires, and waveguides have been fabricated in As_2S_3 by direct laser writing (DLW)[7, 9-12]. The structure and properties of ChG films are known to be sensitive to the deposition method[12]. By exploring certain thermal depositions and processing of As_2S_3, functional properties such as refractive index (*n*) can be controlled and optimized for targeted applications.

This work reports how the structure, morphology, and appearance of nano-structures created by DLW relates to the etch response, deposition rate and chemical composition of the thermally deposited As_2S_3 films in which they are prepared. A standing-wave interference effect is shown to impact the shape of features that can be produced in films up to a thickness of 1 µm. ~~The~~ Chemical compositional variations for UV exposed and unexposed films are correlated to the etch response, nano-structure formation, and deposition conditions of the individual films. The refractive index increase with degree of cross-linking from a UV exposed to laser exposed sample is reported.

2. METHODOLOGY

2.1. Deposition

As_2S_3 was deposited onto polished silicon wafers by thermal evaporation of the bulk glass. Two different deposition rates were used to explore its effect on the film composition and photo-response. The temperature of the substrate was not controlled. Films #1 and #5 were deposited at a rate of 80 Å s^{-1}. Film #1 had a final thickness of 171 nm ± 11 nm and appeared pink in color. Film #5 had a thickness of 204 nm ± 16 nm and appeared blue. Films #2, #3, and #4 were deposited at a rate of 25 Å s^{-1}. Films #2 had a thickness of 204 nm ± 24 nm and appeared pinkish/blue. Films #3 and #4 had a thickness of 170 nm ± 17 nm and 169 nm ± 11 nm, respectively, and both appeared pink. Films #6 was deposited at a rate of 27 Å s^{-1}, had a thickness of 1075 nm ± 0.8 nm, and appeared pink. The films were transported in petri dishes wrapped with aluminum foil and stored in an amber desiccator in a cupboard to prevent unintended exposure to ambient light.

2.2. Photo-patterning

DLW was performed using a continuous-wave mode-locked femtosecond laser (Coherent-Mira, 800-nm center wavelength, 120-fs pulse duration, 76 MHz repetition rate). The film exposure was controlled using a mechanical shutter and the power was controlled using a half-wave plate/polarizer combination. The beam was routed through beam expanders to a 100×/1.4 Numerical Aperture (NA) oil-immersion objective (Nikon) which focused the beam into the film/substrate interface. An arbitrary coordinate system is defined so that the substrate lies in the *xy*-plane and the beam focuses along the *z*-axis. The average power used to cross-link the films was measured at the exit aperture of the objective with an integrating sphere and ranged from 0.05 mW to 0.20 mW. The sample was translated at a speed of 50 µm s^{-1} in the *x*-, *y*-, and *z*-axes relative to the laser beam to define the pattern. Arrays of single-point, nano-scale features were photo-patterned by locating the beam to a targeted (*x*,*y*)-position, opening the shutter, then translating the sample in the *z*-direction over a distance of 6 µm, to ensure that the feature was exposed throughout the entire thickness of the film.

2.3. Etching

To investigate the etch-response, UV-exposed and unexposed films were immersed in ~~a~~ solutions from ~~of~~ 0.05 mol-% to 0.90 mol-% diisopentylamine (DIPA) dissolved in dimethylsulfoxide (DMSO) and monitored visually with a camera to identify the time required to remove both the exposed and unexposed material. UV-exposed films were prepared by irradiating samples for two minutes in a Zeta Loctite UV flood chamber equipped with high-pressure

mercury lamps that emit broad-band UV radiation (65 mW/cm^2). The UV chamber is used to flood-expose a film sample. The etch rate (Eq. 1) is defined as:

$$\text{Etch Rate} = \frac{\text{Film Thickness}}{\text{Etch Duration}} \tag{1}$$

Etch contrast is defined (Eq. 2) as the ratio of times required to remove unexposed and exposed material from the same film type.

$$\text{Etch Contrast} = \frac{\text{Rate (unexp)}}{\text{Rate (exp)}} \tag{2}$$

Photo-patterned arrays of nano-structures were etched using a solution of 0.05 mol-% DIPA in DMSO. The sample was immersed into the etchant for 60 to 300 seconds then rinsed with acetone. After etching, the As_2S_3 structures were imaged by scanning electron microscopy (SEM). The SEM images were used to determine the dimensions and shapes of the features so these could be correlated with film composition and processing conditions.

2.4. Characterization

Micro-Raman spectroscopy was used to investigate the chemical composition of the UV exposed and unexposed films. A Horiba Jobin Yvon LabRamHR high resolution confocal Raman microscope system with an excitation wavelength of 785 nm and an average power of 80 mW at the output was used for the measurements. Special care was taken by adjusting the laser power with an optical density (OD) filter to avoid inducing any unwanted photo-modifications on the As_2S_3 film during the experiment. The incoming laser beam was focused onto the front polished surface of the sample via a 100× microscope objective (*NA* = 0.9, WD = 0.21 mm), with a spatial resolution of 2 microns. A backscattering geometry was used to collect the Raman signal, which, in turn was spectrally analyzed with a spectrometer and an open electrode CCD detector (1024 × 250 chip). The chemical change that results upon DLW was studied by photo-patterning 100 µm × 100 µm square pads, etching away unexposed material, then examining the remaining square pad of As_2S_3 by micro-Raman spectroscopy. Variable-angle ellipsometry (Woollam M2000, 0.24 µm - 1.7 µm) was used to measure the refractive index of unexposed, UV-exposed, and laser-exposed films. Focusing optics were used to characterize regions as small as 100 × 100 µm^2 with a spectral resolution of 3 nm at visible wavelengths and 6 nm in the near infrared.

3. RESULTS AND ANALYSIS

3.1. Etch characteristics

Wong *et al*. reported that solutions of 0.05 mol-% to 5.3 mol-% of DIPA in DMSO can be used to etch thermally deposited As_2S_3 films[7]. Others have reported using solutions of 2 mol-% to 3 mol-% DIPA in DMSO[9,10]. It was observed in this work that DIPA is miscible in DMSO only up to *circa* 1.0 mol-%. At higher targeted concentrations the mixture phase separateds.

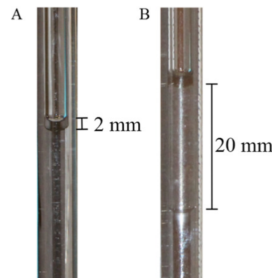

Figure 1. Photos of the immiscible phase that resulted when etchants were prepared to targeted concentrations of (A) 1.96 mol-% and (B) 5.5 mol-% of DIPA in DMSO. The images show the top-layer of the immiscible phase drawn up into a 2 mL pipette for inspection.

Solutions of DIPA in DMSO with targeted concentrations of 0.05 mol-% to 5.5 mol-% were prepared and the upper layer was extracted into 2 mL pipettes and examined for evidence of phase separation. Figure 1 shows that a phase-separated layer was clearly visible at 1.96 mol-% and its volume was greater for the 5.5 mol-% mixture. No phase separation was observed for solutions having targeted concentrations of 0.054 mol-% to 0.9 mol-% DIPA in DMSO. Analysis by ^{1}H NMR confirmed that the lower phase consisted of DMSO saturated in DIPA at 1.6 mol-%, whereas the upper phase was primarily excess DIPA. The etch time and etch contrast were measured for samples of Film #3 using true solutions having DIPA in DMSO at concentrations below 1 mol-%. Figure 2 shows that the etch time rapidly decreases as the concentration of DIPA increases, but approaches a minimum as the DIPA concentration approaches 1.0 mol-%. UV exposed samples from Film #3 were etched in the same solutions and an etch contrast was obtained using Eqn. 2. The etch contrast increases rapidly with DIPA concentration but then also appears to reach a plateau at 1.0 mol–%. The NMR-, etch-time, and etch-contrast data all suggest that the concentration of DIPA in DMSO saturates between 1.6 to 0.5 mol-%. A two phase system was not expected to give consistent post-exposure etching. As a result, all subsequent work was performed using 0.5 mol-% DIPA in DMSO, which is well below the saturation point.

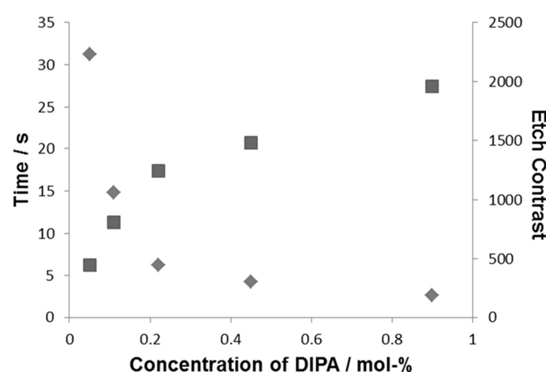

Figure 2. Etch time in seconds (diamonds) and etch contrast (squares) for Film #3 processed using solutions of 0.054 mol-% to 0.9 mol-% DIPA in DMSO.

3.2. Fabricated nano-structure arrays

A set of sixteen arrays, each a 9 × 9 grid of single-point exposures with a 500 nm pitch, were created in each film by DLW over a wide range of average (avg) focused laser powers (0.05 mW avg to 0.425 mW avg) and etched with 0.5 mol-% DIPA in DMSO solution. When the laser power was too low, sufficient cross-linking did not occur and the resulting nano-scale features would either not be robust enough to survive etching or they would delaminate during the solution processing. The lowest power at which intact feature are observed is referred to hereafter as the minimum power limit. Above this limit, robust features were formed with dimensions that increased steadily with laser power. If the laser power was too high, adjacent nano-structures would become large enough to overlap. The greatest power at which distinct features could be observed is referred to hereafter as the maximum power limit. The range of powers over which robust free-standing nano-structures could be formed was measured for each film and correlated with thickness, etch contrast, and morphology.

Figure 3 shows top and profile views of nano-scale features fabricated in each of Films #1 - #6. The structures' widths along the *x*- and *y*-directions were measured for each array and film from the minimum to maximum power limits. Table 1 shows thickness and deposition rates in relation to shape, etch contrasts, and structure size for each film. The *x*- and *y*-widths of the features are not expected to be exactly the same because a linearly polarized beam focused under high numerical aperture does not generate a rotationally symmetric point spread function[13,14]. However, this effect is not expected to cause the widths to differ by more than 10%.

All films were found to have a narrow power range over which viable structures could be patterned without delaminating or overlapping (Fig. 4). Structures were only formed within powers of 0.050 mW to 0.225 mW for all films. Feature size is found to increase with fabrication power as expected; however, as the features become smaller with lower power, they are more susceptible to delamination during development. The smallest feature sizes were found in the

films with the highest deposition rate (Films #1 & #5; 80 Å s^{-1}). Although these same films (#1 & #5) differ in thickness by 33 nm, exhibit different etch rate and contrast, and yield nano-structures with different shapes**;** they ~~did~~ produced features with similar minimum sizes at similar lower power limits. The films produced with low deposition rate (Films #2, #3, #4; 25 Å s^{-1}) differed in thickness by 35 nm, exhibited variable etch rate and contrast, and yielded highly variable feature shape, dimensions, and minimum- and maximum- power limits. These differences suggest that high deposition rate produces films that are more compositionally uniform. In any case, films produced with high deposition rate do appear to yield patterned features with more similar power-size dependence and better adhesion.

Etch rate and contrast are shown in Table 1 to give insight into how etch selectivity relates to film properties. Etch rate depends on the films' etch duration, which was determined by recording the time required for the film to dissolve completely in the etchant. For unexposed films, this time was less than one minute. A video recording was made of the entire etch process and then analyzed frame by frame to obtain accurate values for the etch duration. For UV exposed films, the etch duration normally required several hours, and the film did not completely dissolve. Rather, it tended to delaminate from the substrate leaving fragments of material in the solution. The time at which the films were observed to begin delaminating at the corners was taken as the etch time for UV exposed films. Although both the unexposed etch rate and etch contrast are given in Table 1, the UV exposed etch durations are only intended to provide a semi-quantitative measure of etch selectivity and are not expected to be as accurate as the etch durations of unexposed films.

The lowest values for etch rate and contrast are seen for Films #2 and #5. Films #2 and #5 have similar thicknesses, feature shapes, and fabrication power limits. The highest values for etch rate and contrast are seen for Films #1, #3, and #4, which have similar thicknesses and feature shapes but varying fabrication power limits. Deposition rates were not observed to correlate with etch rate or contrast. Dome shaped features are formed in thicker films with low etch contrasts (Films #2 and #5); whereas oblate-shaped features formed in thinner films with high etch contrasts (Films #1, #3, #4). When the etch rate and contrast is high, the variation in cross-linking is resolved by the etchant, yielding oblate structures. On the contrary, when the etch rate and contrast is low, the cross-linked material closest to the substrate is not resolved the by etchant, yielding dome structures. The dome shape may also explain how the small features fabricated on Film #5 did not delaminate.

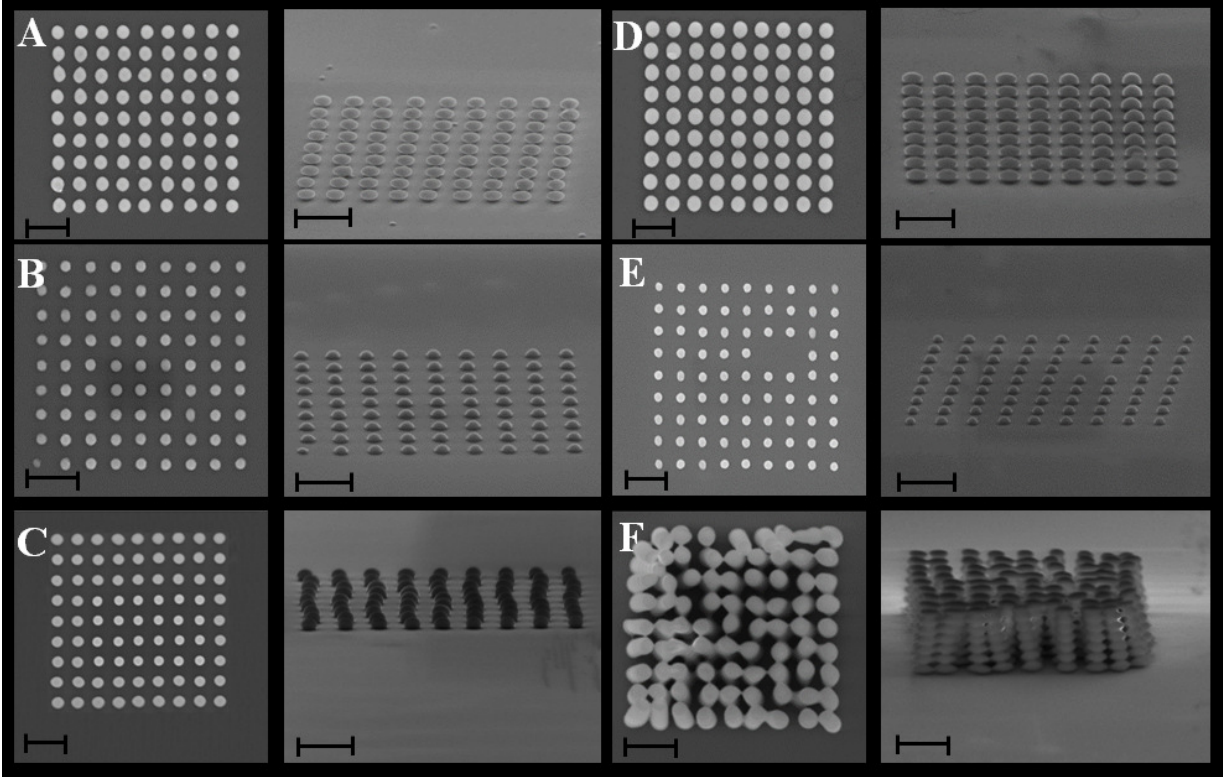

Figure 3. Frames A through F show top- and profile-views of nano-scale features fabricated in thermally deposited As_2S_3 Films #1 - #6, respectively. The scale bar corresponds to 1 µm.

Figure 3F shows that fabrication in Film #6 yielded stacks of nano-scale beads in an array, rather than cylindrical pillars as expected. The appearance of these features suggests that the focused beam reflects at the silicon substrate back into the interaction volume producing standing wave interference that modulates the film exposure with distance from the substrate. In this case, the interference maxima for antiparallel interfering light should occur along the direction of beam propagation, separated by distance d_{max} given by

$$d_{max} = \frac{\lambda}{2n}, \tag{3}$$

where λ is the wavelength of the excitation beam, and n is the refractive index of the film. The result then is that distance between the "nano-beads" in a stack and the number of beads formed within a given film should depend on the wavelength of the excitation beam. To test this hypothesis, fabrication was repeated at 720 nm, 800 nm, and 900 nm to confirm the influence of standing wave interference on the feature shape.

Figure 5 summarizes the observed effect of varying the excitation wavelength when fabricating in Film #6. As λ increases from 720 nm, to 800 nm, and then 900 nm, the center-to-center distance between beads increases from 140 ± 5 nm, to 171 ± 3 nm, and finally 198 ± 5 nm. Correspondingly, the number of beads within the stacks decreases with excitation wavelength from 8 to 7 to 6. Figure 6 shows the observed distance between beads versus λ, as well as that predicted using Eqn. 3. For this calculation, the values for the refractive index were obtained by ellipsometry (discussed below) and were taken as $n = 2.56$, 2.50, and 2.48 for $\lambda = 720$ nm, 800 nm, and 900 nm, respectively. The measured and predicted bead separations are in good agreement. Additionally, because the refractive index of the As_2S_3 film ($n_{film} \sim 2.5$) is less than that of the substrate ($n_{Si} > 3.5$), the reflected wave is antiphase with the incident beam, leading to destructive interference at the substrate and constructive interference at distance $d_{max}/2$ from the interface. The ratio of reflected to incident field amplitudes should be on the order of $[(n_{Si} - n_{film})/(n_{Si} - n_{film}) = 0.17$, resulting in large exposure

modulation. This results in significant under-exposure immediately at the substrate and at multiples of d_{max} from the interface, consistent with the form of the nano-structures seen in Figs. 3f and 5.

Table 1. Film deposition conditions and thickness as they relate to etch-contrast and size and shape of nano-scale features generated in that film by DLW.

Film #	Feature shape	Deposition rate / Å s^{-1}	Thickness / nm	Unexposed etch rate / nm s-1	Etch contrast	Feature size at minimum power limit			Feature size at maximum power limit		
						x-width / nm	*y*-width / nm	Power / mW	*x*-width / nm	*y*-width / nm	Power / mW
1	Oblate	80	171 ± 11	23.6 ± 6	2580	204 ± 7	226 ± 8	0.075	497 ± 29	506 ± 23	0.175
2	Dome	25	204 ± 24	13.6 ± 2	779	206 ± 18	222 ± 20	0.050	463 ± 15	506 ± 21	0.125
3	Oblate	25	170 ± 17	40.0 ± 8	3868	286 ± 12	292 ± 9	0.100	430 ± 37	440 ± 35	0.200
4	Oblate	25	169 ± 11	34.6 ± 4	2862	344 ± 9	396 ± 16	0.150	497 ± 29	502 ± 25	0.225
5	Dome	80	204 ± 16	3.5 ± 1	259	188 ± 11	220 ± 12	0.075	482 ± 18	497 ± 14	0.175
6	Oblate	27	1075 ± 0.8	19.6 ± 1	343	320 ± 16	328 ± 29	0.175	377 ± 29	388 ± 32	0.225

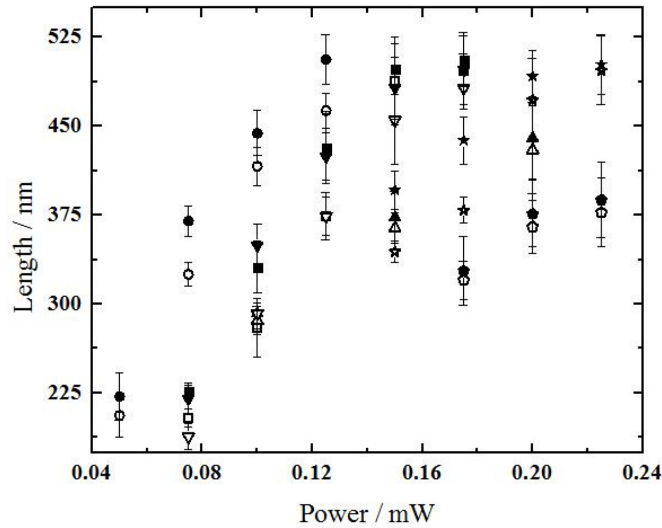

Figure 4. *X*-width (filled shapes) and *y*-width (open shapes) measurements for Film #1 (squares), Film #2 (circles), Film #3 (up triangles), Film #4 (stars), Film #5 (down triangles) and Film #6 (pentagons) versus power.

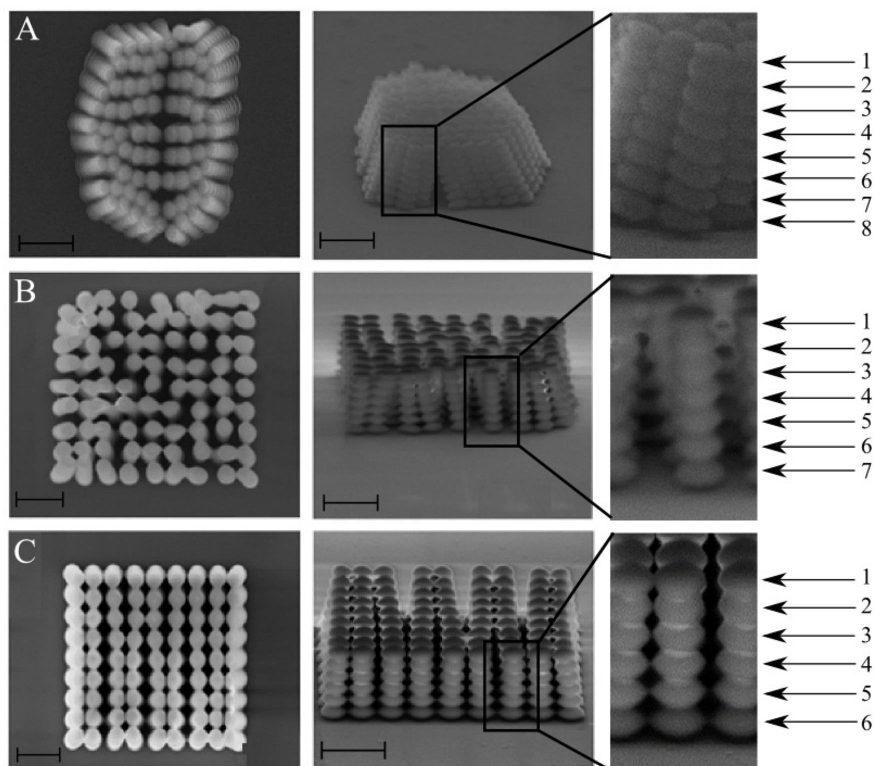

Figure 5. SEM top down and profile images of nano-bead structures fabricated in Film #6 at fabrication wavelengths of 720 nm (A), 800 nm (B), and 900 nm (C). Magnified nano-bead structures are shown with bead counts for each fabrication wavelength. The scale bar is equals 1 µm.

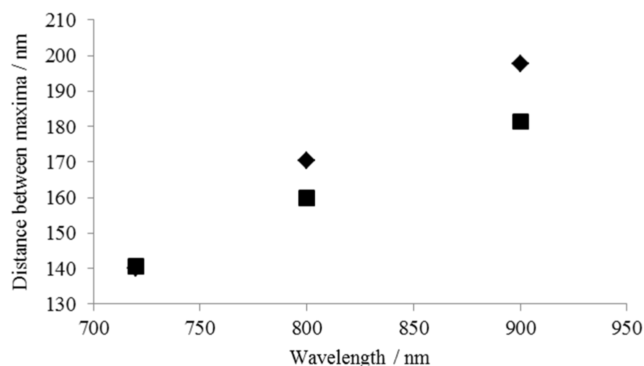

Figure 6. Measured (diamonds) and expected (squares) distance between interference maxima using laser fabrication wavelengths of 720 nm, 800 nm, and 900 nm.

3.3. Micro-Raman characterization of unexposed and exposed films

Micro-Raman spectroscopy was used to identify the presence of molecular fragments in unexposed and UV-exposed films and to investigate the variation of chemical compositional across the entire Film #6 wafer. Bulk As_2S_3 is a glassy network solid[7]. Thermal deposition fragments the As_2S_3 network producing numerous molecular clusters, such as As_4S_6, As_4S_4, and S_8. These deposit onto the substrate forming a metastable glassy film that can be photo-cross-linked back to the As_2S_3 network by photoexcitation[7]. Films that are rich in As_4S_6, As_4S_4, S_8, and other clusters containing

homopolar As-As and S-S bonds, are known to exhibit the highest photosensitivity. These bonding arrangements are effectively structural defects that lower the density, refractive index, and stability of thermally deposited films relative to bulk As_2S_3[12].

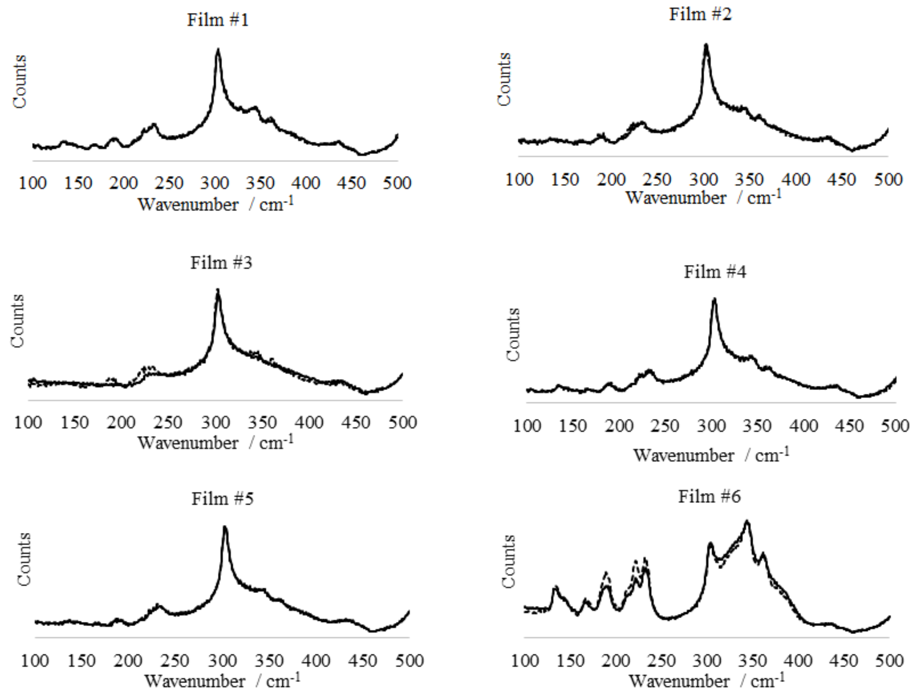

Figure 7. Raman spectra of UV exposed (solid line) and unexposed (dashed line) films for all films.

Raman spectra from all UV-exposed and unexposed films are presented in Fig. 7. The peaks were assigned as described in Reference 7. A broad peak at 348 cm^{-1} indicates the presence all three heteropolar fragments (especially As_4S_6). Peaks at 232 cm^{-1} and 136 cm^{-1} are As_2S_3 glass, and peaks at 222 cm^{-1} are the As_4S_4 subunits. Low frequency peaks (190, 225, 235 cm^{-1}) are assigned to As_4S_4 cage molecules and As-As homopolar bonds. The broadband peak at 345 cm^{-1} is associated with As-S-As stretching vibration. The peak around 494 cm^{-1} is associated with S-S homopolar bonds. The large, sharp peak at 300 cm^{-1} is due to the silicon substrate.

Relative to Film #6, films #1 - #5, which all had thicknesses of approximately 200 nm, had peaks of similar intensity indicating the presence of As_4S_4 cage molecules and As-As homopolar bonds as well as As-S-As stretching vibrations. This implies that the unexposed films were very similar in chemical composition despite their different deposition rates. Although UV exposure is expected to cause the As_4S_4 peaks to decrease and the As_2S_3 peaks to increase as the material photo-cross-links, no such change was observed when Films #1, #2, #4 and #5 were UV-exposed, even though they were observed to resist etching in DIPA/DMSO. This suggests that the low UV-exposure used sufficiently cross-linked the material to make it resist etching, but not enough bonds were converted to enable detection by Raman spectroscopy. The As_4S_4 and As_2S_3 peaks did change significantly with UV exposure of Film #3, which also had the highest etch contrast among all films as seen in Table 1. This indicates that Film #3 may have a slight variation in composition from the other films which allowed for a faster etch rate of unexposed film and a higher degree of cross-linking (slower etch rate) in exposed films.

The 1 µm thick film (Film #6) spectra contained more peaks as well as a more distinguished spectral difference between UV exposed and the unexposed film than Films #1 - #5 (Fig. 7). This was most likely because Film #6 is much thicker than the others, which provides greater Raman interaction path length and improved signal to noise. Therefore, film peaks are more comparable to the peak from the silicon substrate and detection of small changes is easier. This also

implies that the thickness as well as the etch contrast play a major role in the determination of degree of cross-linking through Raman spectral analysis. A closer look at Film #6 reveals that while many of the peaks diminish after UV exposure, the ratio of homopolar to heteropolar bonds changes to a greater extent than the AsS_3 peaks (233 cm^{-1} / 222 cm^{-1}) (Fig. 8). The shoulder at 380 to 400 cm^{-1}, which is associated with the As-S-As bridges, increased as well. The difference in ratio of homopolar to heteropolar bonds is significant because a decrease in As_4S_4 with an increase in As_2S_3 molecules indicates cross-linking. Film #6 shows clear signs of chemical cross-linking after UV flood exposure based on Raman peaks analysis (Fig. 8).

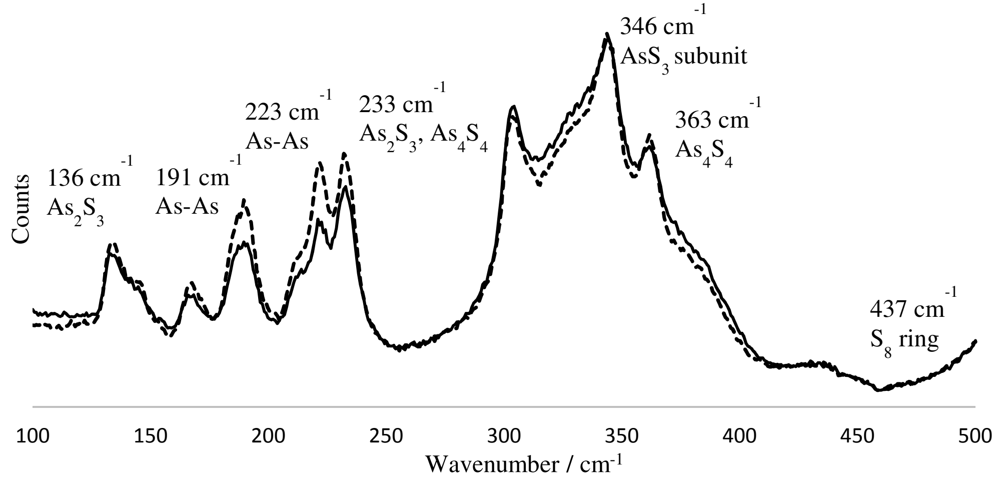

Figure 8. Raman spectra of UV exposed (solid line) and unexposed (dashed line) Film #6 with peaks identified.

Zoubir and co-workers studied the chemical and structural composition of thermally deposited As_2S_3 films through Raman measurements and examined how these features changed upon laser exposure[15]. Our Raman spectra of Film #6 showed a similar decrease in the low frequency peaks (190, 225 and 235 cm^{-1}) associated with As-As, As_2S_3, and As_4S_4 molecules after UV exposure; however, our spectral differences were less apparent and did not ~~lacked the~~ decrease near ~~around~~ the 494 cm^{-1} peak[15]. This difference between our data and the referenced data may come from the difference in Raman excitation wavelength (785 nm vs. 840 nm) and exposure conditions (UV flood exposure vs. femtosecond laser exposure). The intensity of the Raman signals depends upon the excitation wavelength and proximity of electronic transitions within the material. And UV exposure could produce more uniform exposure throughout the film than is achieved with scanned-beam femtosecond laser exposure.

In order to determine chemical variation across a large area, Raman spectra were collected from various positions including edges and the center of the Film #6 wafer. To test if the film was being cross-linked by the Raman laser, three successive spectra were collected at each of the measurement positions within the sample. As shown in Table 2, the ratio of peaks associated with As_2S_3 glass (232 cm^{-1} and 136 cm^{-1}) and As_4S_4 clusters (222 cm^{-1}) increases slightly with each collected spectrum. This indicates that the Raman excitation laser at 785 nm does cause some cross-linking in the film. It is noteworthy that these ratios vary somewhat across the films, but not enough to suggest there was major composition variation within the film.

Table 2. Raman characterization of ChG film cross-linking as a function of position in a representative film and versus Raman-spectrum acquisition number.

Position	Scan #	$\frac{\text{Counts at 232 cm}^{-1}}{\text{Counts at 222 cm}^{-1}}$	$\frac{\text{Counts at 136 cm}^{-1}}{\text{Counts at 222 cm}^{-1}}$	Position	Scan #	$\frac{\text{Counts at 232 cm}^{-1}}{\text{Counts at 222 cm}^{-1}}$	$\frac{\text{Counts at 136 cm}^{-1}}{\text{Counts at 222 cm}^{-1}}$
A	1	0.990	0.848	D	1	1.031	0.879
	2	1.043	0.994		2	1.077	1.030
	3	1.061	1.046		3	1.123	1.107

B	1	1.006	0.862	E	1	0.979	0.819
	2	1.028	0.996		2	1.018	0.935
	3	1.071	1.056		3	1.058	0.985
C	1	0.987	0.826	F	1	0.986	0.790
	2	1.038	0.961		2	1.003	0.832
	3	1.038	1.009		3	1.042	0.913

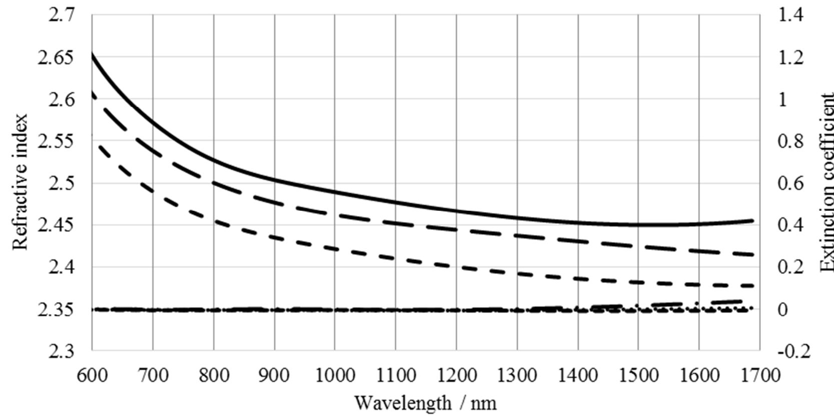

Figure 9. Refractive index *n* of the laser exposed film (solid line), UV exposed film (large dashed line) and unexposed film (medium dashed line). Extinction coefficient *k* of the laser exposed film (dashed and dotted line), UV exposed film (small dashed line), and unexposed film (dotted line).

3.4. Refractive index measurements of material with and without photo-exposure

Ellipsometry was used to determine the refractive index *n* and extinction coefficient *k* for the 1 µm thick Film #6 with and without exposure. A 250 µm × 250 µm square pad was created in Film #6 by DLW. The probe wavelengths span from 240 nm to 1687 nm. Analysis showed that a SiO_2 native oxide layer was present on the surface with a thickness of 3.7 nm. This value was used as a constant throughout all subsequent analyses. A "B-Spline" layer was used to simulate the As_2S_3 film layer. This layer allows for arbitrary *n* and *k* values but also considers values of neighboring wavelengths to give a smoother and more realistic dispersion curve. Free parameters included thickness, surface roughness, and substrate back reflection. The values obtained for *n* and *k* of the As_2S_3 layer were found to be consistent in terms of their respective Kramers-Kronig transforms when only the imaginary part of the dielectric constant is allowed to vary.

The *n* and *k* values are plotted over a wavelength range of 600 nm to 1687 nm in Fig. 10. UV exposure increases the refractive index by roughly 0.05 units over that of the pristine film, consistent with the increase in polarizability that results upon cross-linking to the network solid. Laser exposure increases the refractive index more, by roughly 0.07 units at all wavelengths. This suggests that laser exposure achieves a higher degree of cross-linking throughout the depth of the film. There exists a slight increase near 1600 nm in *n* and *k* values of the laser exposed film due to a high degree of noise in psi and delta. The dispersion curves for the unexposed and laser exposed films are similar to others reported in the literature; though the literature curve is slightly lower[16].

4. CONCLUSIONS

The morphology, size, and appearance of nano-structures are studied in relation to etch response, fabrication power limits, deposition rate, and chemical composition of the thermally deposited As_2S_3 films. The etching solution DIPA in DMSO was found to be phase separated for targeted concentrations greater than 1.0 mol-%, and subsequent etches were done using 0.5 mol-%. Thermally deposited films were found to be photo-patternable by multi-photon direct laser writing (DLW). Thermal deposition rates of 25 Å s^{-1} and 80 Å s^{-1} were found to produce highly photoactive films that could yield nano-structures. There was no clear correlation of observables with deposition rate, however; thicker films with low etch rates and contrasts yielded dome shaped features (as compared to oblate shaped features found in high etch rate and contrast films) with the smallest minimum power widths. There was no significant evidence for compositional variation within the films. Ellipsometry shows *n* increases with exposure, which is consistent with prior results. A higher degree of cross-linking was achieved with laser exposure over that found with UV exposure, as evinced by higher index. Novel nano-bead structures were created as a result of standing wave interference effect in the 1 µm thick film.

5. ACKNOWLEDGEMENTS

This work was partially supported by NSF CAREER award DMR/CHE-0748712; Lockheed Martin Missiles and Fire Command; the Florida High Tech Corridor Council; the Space Research Initiative Program, through the Florida Space Institute hosted at the University of Central Florida; and the National Aeronautics and Space Administration through the University of Central Florida's NASA-Florida Space Grant Consortium. AML was supported by a UCF SURF Scholarship. We thank Dr. Pieter Kik and Mr. Chatdanai Lumdee for assistance with the ellipsometry measurements.

6. REFERENCES

[1] Moreshead, W. V., Novak, J. and Symmons, A., "An Investigation of Material Properties for a Selection of Chalcogenide Glasses for Precision Glass Molding." Proc. of SPIE, 8541(2012).
[2] Zhang, X.H. Guimond, Y. and Bellec Y., "Production of complex chalcogenide glass optics by molding for thermal imaging." J.Non-Cryst.Solids, 326: p. 5. (2003).
[3] Cha, D. H., Kim, H. J., Park, H. S., Hwang, Y., Kim, J. H, Hong, J. H, and Lee, K. S, "Effect of temperature on the molding of chalcogenide glass lenses for infrared imaging applications." Appl. Opt., 49(9): p. 1607. (2010).
[4] Cha, D. H., Kim, H. J., Hwang, Y., Jeong, J. C. and Kim, J.H., "Fabrication of molded chalcogenide-glass lens for thermal imaging applications." Appl. Opt., 51(23): p. 5649. (2012).
[5] Ma, K. J., Chien, H. H., Huang, S. W., Fu, W. Y. and Chao, C. L., "Contactless molding of arrayed chalcogenide glass lenses." J.Non- Cryst.Solids, 2011. 357: p. 2484 (2011).
[6] R´odenas, A., Martin, G., Arezki, B., Psaila, N., Jose, G., Jha, A., Labadie, L., Kern, P., Kar, A. and Thomson, R., "Three-dimensional mid-infrared photonic circuits in chalcogenide glass," Opt. Lett. 37, 392–394 (2012).
[7] Wong, S., Deubel, M., Pérez-Willard, F., John, S., Ozin, G. A., Wegener, M. and Freymann, G. v., "Direct Laser Writing of Three-Dimensional Photonic Crystals with a Complete Photonic Bandgap in Chalcogenide Glasses." Adv. Mater, 18: p. 5. (2006).
[8] Kuebler, S. and Rumi, M., "Nonlinear optics applications- Three-Dimensional Microfabrication. Encyclopedia of Modern Optics." p. 189-206. (2004).
[9] Nicoletti, E., Zhou, G., Jia, B., Ventura, M. J., Bulla, D., Luther-Davies, B. and Gu, M., "Observation of multiple higher-order stopgaps from three-dimensional chalcogenide glass photonic crystals," Opt. Lett. 33, 2311–2313 (2008).
[10] Nicoletti, E., Bulla, D., Luther-Davies, B. and Gu, M., "Wide-angle stop-gap chalcogenidephotonic crystals generated by direct multiple-line laser writing," Appl. Phys. B 105, 847–850 (2011).
[11] Nicoletti, E., Bulla, D., Luther-Davies, B. and Gu, M., "Generation of λ/12 nanowires in chalcogenide glasses," Nano. Lett., 11, 4218–4221 (2011).
[12] Choi, D., Madden, S., Bulla, D., Wang, R., Rode, A. and Luther-Davies, B., "Thermal annealing of arsenic trisulphidethin film and its influence on device performance," J. Appl. Phys. 107, 053106 (2010).
[13] Sun, H.B., Maeda, M., Takada, K., Chon, J. W. M., Gu, M., and Kawata, S., "Experimental investigation of single voxels for laser nanofabrication via two-photon photopolymerization. "Appl. Phys. Lett., 83(5) (2003).
[14] Cumming, B. P., Debbarma, S., Luther-Davies B. and Gu, M., "Effect of refractive index mismatch aberration in

arsenic trisulfide," Appl. Phys. B 109, 227–232 (2012).
[15] Zoubir, A., Richardson, M., Rivero, C., Schulte, A., Lopez, C., Richardson, K., Ho, N. and Vallee, R., "Direct femtosecond laser writing of waveguides in As_2S_3 thin films." Opt. Lett., 29(7): p. 3. (2004).
[16] Petkov, K., "Compositional dependence of the photoinduced phenomena in thin film chalcogenide films" Journal of Optoelecrtonics and Advanced Materials, Vol. 4, No. 3, p. 611 – 629 (2002).